Ocean Engineering 288 (2023) 115893

Contents lists available at ScienceDirect

Ocean Engineering

journal homepage: www.elsevier.com/locate/oceaneng

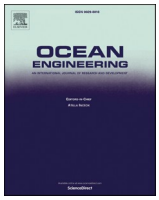

Numerical investigation of wave-cylinder interaction based on a momentum source wave generation method

Hou-sheng Zhang [a], Biao Huang [b], Xin Zhao [a,*]

[a] School of Aerospace Engineering, Beijing Institute of Technology, Beijing, 100081, China
[b] School of Mechanical Engineering, Beijing Institute of Technology, Beijing, 100081, China

ARTICLE INFO

Handling editor: A.I. Incecik

Keywords:
Wave generation
Momentum source function
Regular wave
Irregular wave
Wave load

ABSTRACT

A momentum source function is constructed for wave generation based on linear wave theory. Based on Navier-Stokes equation and volume of fluid (VOF) method, a three-dimensional numerical wave tank (NWT) is established. Regular and irregular waves can be simulated by applying the momentum source function to NWT, and the expected wave characteristic parameters and wave spectrum are obtained. Furthermore, the load characteristics of two types of cylinders, fully piercing cylinder (FPC) and truncated cylinder (TC), are studied under regular wave field combined with boundary data immersed method (BDIM). Results show that the transverse force exerted on cylinders is dominated by inertial force. And because of the effects of the cylinder on wave profile and drag force, the maximum transverse force occurs soon after the wave node passes through the centerline of the cylinder. Compared with the FPC, the drag force has a greater influence on TC.

1. Introduction

Numerical wave tank (NWT) is an important tool to study the characteristics of water waves and the interaction between water waves and structures. At present, most NWT is based on viscous Navier-Stokes equations (Choi and Yoon, 2009; Guo et al., 2012; Lin and Liu, 1999; Martínez-Ferrer et al., 2018; Perić and Abdel-Maksoud, 2015; Wang and Gao, 2022) or potential flow theory (Ben-long and Hua, 2005; Benxia et al., 2004; Dommermuth and Yue, 1987; Houtani et al., 2018; Wei et al., 1999; West et al., 1987; Xu et al., 2022). Laplace equation is considered as the governing equation for NWT based on potential flow theory, which has a long history and is relatively mature at present. However, when the fluid viscosity cannot be ignored, especially in the wave-structure interaction (WSI) where the viscous effect is important, the NWT based on potential flow theory can no longer meet the demand. With computational performance continuously improving, the viscous NWT has gradually been further studied and widely used.

Wave generation method mainly includes the physical wave generation method (such as moving boundary method), setting generation boundary, setting generation region where the velocity or other parameters are designated, and the source function method. The source function method is divided into mass source function method and momentum source function method. Lin and Liu (1999) established a NWT based on a mass source function from the continuity equation, and by using different mass source functions, linear regular waves, irregular waves, Stokes waves, solitary waves and elliptical cosine waves can be realized. Based on Boussinesq models, Wei et al. (1999) proposed a mass source function that can effectively simulate regular and random waves, and further derive the source function for momentum equation. Furthermore, Choi and Yoon (2009) and Ha et al. (2013) applied Wei's internal wave maker to three-dimensional viscous NWT using the momentum source function, and the expected regular and irregular waves are produced. Wang and Gao (2022) combined velocity-inlet boundary with momentum source function based on fifth-order Stokes wave theory to ensure the accuracy of waves propagation, and the effectiveness of wave generation with different steepness is verified.

In this paper, a momentum source function for regular and random waves generation method are proposed based on linear water wave theory, and the NWT is established by combining the three-dimensional viscous Navier-Stokes equations and VOF method. Regular waves with different wave parameters and random waves based on JONSWAP spectrum are simulated. Finally, combined with the boundary data immersion method (IBM), the transverse force characteristics of the cylinder under regular wave conditions are simulated.

* Corresponding author.
E-mail address: 6120160101@bit.edu.cn (X. Zhao).

https://doi.org/10.1016/j.oceaneng.2023.115893
Received 10 April 2023; Accepted 19 September 2023
Available online 10 October 2023

2. Numerical model

2.1. Mathematical model

The impressible viscous Navier-Stokes equation is adopted to solve the wave field:

$$\nabla \cdot \boldsymbol{U} = 0 \tag{1}$$

$$\frac{\partial \boldsymbol{U}}{\partial t} + (\boldsymbol{U} \cdot \nabla)\boldsymbol{U} = -\frac{1}{\rho}\nabla p + \mu \nabla \cdot (\nabla \boldsymbol{U}) + \boldsymbol{g} + \boldsymbol{f}_{\sigma} + \boldsymbol{f}_{w} + \boldsymbol{f}_{d} \tag{2}$$

where, $\mathbf{U} = [u, v, w]$ is the velocity vector, p denotes pressure, $\mathbf{g}$ represents gravitational acceleration, $\mathbf{f}_{\sigma}$ is the surface tensor, $\mathbf{f}_{w}$ is the momentum source function for wave generation, $\mathbf{f}_{d}$ is the momentum source function for wave absorbing. ρ and μ denote mixing density and dynamic viscosity respectively, and the mixing parameters are defined as

$$\rho = \alpha_l \rho_w + (1 - \alpha_l)\rho_a \tag{3}$$

$$\mu = \alpha_l \mu_w + (1 - \alpha_l)\mu_a \tag{4}$$

where, ρ_w and ρ_a are the density of water and air respectively, and α_l is the volume fraction of water.

The VOF method (Tryggvason et al., 2006) is applied to capturing the gas-liquid interface and the advection of the volume fraction function is governed by

$$\frac{\partial \alpha_l}{\partial t} + \boldsymbol{U} \cdot \nabla \alpha_l = 0 \tag{5}$$

2.2. Momentum source function

The velocity potential function based on linear theory of surface gravity waves is (Dean and Dalrymple, 1991)

$$\varphi = \frac{Ag}{\omega}\frac{cos\ hk(h+y)}{cos\ hkh} sin(kx - \omega t) \tag{6}$$

where, h is the water depth, k denotes wave number, A is the wave amplitude, g is the gravitational acceleration, ω is the angular frequency, x is the direction along which wave propagate, y is the vertical coordinate of NWT and $y = 0$ represents the static water surface.

According to Equation (6), the fluid velocities of wave field could be derived by

$$u_w = \frac{\partial \varphi}{\partial x} = \frac{Akg}{\omega}\frac{cos\ hk(h+y)}{cos\ hkh} cos(kx - \omega t) \tag{7}$$

$$v_w = \frac{\partial \varphi}{\partial y} = \frac{Akg}{\omega}\frac{sin\ hk(h+y)}{cos\ hkh} sin(kx - \omega t) \tag{8}$$

Further, the fluid acceleration is the derivative of velocity with respect to time:

$$f_x = \frac{du_w}{dt} = \frac{\partial u_w}{\partial t} + \boldsymbol{U}_w \cdot \nabla u_w = Akg\frac{cos\ hk(h+y)}{cos\ hkh} sin(kx - \omega t) + \boldsymbol{U}_w \cdot \nabla u_w \tag{9}$$

$$f_y = \frac{dv_w}{dt} = \frac{\partial v_w}{\partial t} + \boldsymbol{U} \cdot \nabla v_w = -Akg\frac{sin\ hk(h+y)}{cos\ hkh} cos(kx - \omega t) + \boldsymbol{U}_w \cdot \nabla v_w \tag{10}$$

where $\mathbf{U}_w = [u_w, v_w]$.

For still water, the momentum source function in the form of gravity wave acceleration f_x and f_y can be introduced into the N–S equation to force the still wave surface to generate motion. Under the assumption of small amplitude, the convection term is relatively small and can be ignored. Therefore, the momentum source function for wave generation is taken as

$$f_{wx} = \frac{\partial u_w}{\partial t} = Akg\frac{cos\ hk(h+z)}{cos\ hkh} sin(kx - \omega t) \tag{11}$$

$$f_{wz} = \frac{\partial w_w}{\partial t} = -Akg\frac{sin\ hk(h+z)}{cos\ hkh} cos(kx - \omega t) \tag{12}$$

The dispersion relationship is given by

$$\omega^2 = kg\tanh(kh) \tag{13}$$

2.3. Wave absorbing method

At the exit of the NWT, a wave absorber zone is set to eliminate the wave to avoid the influence of reflected water wave from outlet boundary on the upstream wave field. The momentum source function for wave absorbing is given by

$$\boldsymbol{f}_d = -C(x)\boldsymbol{U} \tag{14}$$

where $C(x)$ is the damping coefficient (Wei and Kirby, 1995),

$$C(x) = \alpha\frac{exp\left[\left(\frac{x - x_{in}}{x_{out} - x_{in}}\right)^n\right] - 1}{exp(1) - 1} \quad x_{in} < x < x_{out} \tag{15}$$

where, x_{in} and x_{out} are the inlet coordinate and outlet coordinate of the wave absorber zone respectively. And α and n are the empirical parameters determined by numerical tests (Ha et al., 2013; Lin and Liu, 2004). The damping coefficient is only defined in the wave absorber zone and is always zero outside the absorber zone. In this study, the empirical parameters are taken as $n = 10$ and $\alpha = 200$ (Lin and Liu, 2004). The length of the wave absorber zone is set $1.5L$, where L is the wavelength.

2.4. Boundary data immersion method

Boundary data immersion method (BDIM) (Weymouth and Yue, 2011) is adopted to simulate the wave-structure interaction. The meta-equation defined over full domain is constructed by

$$M_{\varepsilon} \equiv B_{\varepsilon}(\Psi_{\varepsilon}) + F_{\varepsilon}(\Psi_{\varepsilon}) + S_{\varepsilon}(\Psi_{\varepsilon}) = 0 \tag{16}$$

where Ψ_{ε} is any physical quantity related to space and time in the whole solution domain. $B_{\varepsilon}(\Psi_{\varepsilon})$, $F_{\varepsilon}(\Psi_{\varepsilon})$ and $S_{\varepsilon}(\Psi_{\varepsilon})$ are defined by

$$\begin{aligned} B_{\varepsilon}(\Psi, \boldsymbol{x}, t) &= \int_{\Omega_b} B(\Psi, \boldsymbol{x}_b, t) K_{\varepsilon}(\boldsymbol{x}, \boldsymbol{x}_b) d\boldsymbol{x}_b F_{\varepsilon}(\Psi, \boldsymbol{x}, t) \\ &= \int_{\Omega_f} F(\Psi, \boldsymbol{x}_f, t) K_{\varepsilon}(\boldsymbol{x}, \boldsymbol{x}_f) d\boldsymbol{x}_f S_{\varepsilon}(\Psi, \boldsymbol{x}, t) = \int_{\sigma_s} S(\Psi, \boldsymbol{x}_f, t) K_{\varepsilon}(\boldsymbol{x}, \boldsymbol{x}_s) d\boldsymbol{x}_s \end{aligned} \tag{17}$$

where $B = 0$ and $F = 0$ are the governing equations in solid domain Ω_b and fluid domain Ω_f respectively. And $S = 0$ are the interfacial conditions on interface σ_s. K_{ε} is the delta integration kernel and satisfies,

$$\int_{\Omega} K_{\varepsilon}(\boldsymbol{x}, \boldsymbol{y}) d\boldsymbol{y} \equiv 1$$

$$K_{\varepsilon}(\boldsymbol{x}, \boldsymbol{y}) \equiv 0, |\mathbf{x}, \mathbf{y}| > \varepsilon \tag{18}$$

The governing meta-equation M_{ε} is constructed by the immersion data immersion method by convoluting and assembling the fluid governing equation, rigid-body equation and the body boundary condition over a width ε. The transition between those equations is smooth and located within the small distance ε of the interface σ_s.

Considering the main contribution in the kernel K_{ε}, Equation (17) can be simplified to

$$B_\varepsilon(\Psi_\varepsilon,\boldsymbol{x},t)\approx B(\Psi_\varepsilon,\boldsymbol{x},t)\int_{\Omega_b}K_\varepsilon(\boldsymbol{x},\boldsymbol{x}_b)d\boldsymbol{x}_b$$

$$=B(\Psi_\varepsilon,\boldsymbol{x},t)\delta_\varepsilon^B(\boldsymbol{x},t)$$

$$F_\varepsilon(\Psi_\varepsilon,\boldsymbol{x},t)\approx F(\Psi_\varepsilon,\boldsymbol{x},t)\int_{\Omega_f}K_\varepsilon(\boldsymbol{x},\boldsymbol{x}_f)d\boldsymbol{x}_f$$

$$=F(\Psi_\varepsilon,\boldsymbol{x},t)\delta_\varepsilon^F(\boldsymbol{x},t)$$

$$S_\varepsilon(\Psi_\varepsilon,\boldsymbol{x},t)\approx S(\Psi_\varepsilon,\boldsymbol{x},t)\int_{\sigma_s}K_\varepsilon(\boldsymbol{x},\boldsymbol{x}_s)d\boldsymbol{x}_s$$

$$=S(\Psi_\varepsilon,\boldsymbol{x},t)\delta_\varepsilon^S(\boldsymbol{x},t) \tag{19}$$

Therefore, Equation (16) can be transformed to

$$M_\varepsilon(\Psi_\varepsilon)\equiv\delta_\varepsilon^B B(\Psi_\varepsilon)+\delta_\varepsilon^F F(\Psi_\varepsilon)+\delta_\varepsilon^S S(\Psi_\varepsilon)=0 \tag{20}$$

The no-slip boundary condition is applied and the meta-equation can be further simplified to

$$M_\varepsilon(\Psi_\varepsilon)\equiv\delta_\varepsilon^B B(\Psi_\varepsilon)+\left(1-\delta_\varepsilon^B\right)F(\Psi_\varepsilon)=0 \tag{21}$$

where, solid domain is governed by

$$B(\boldsymbol{U})=\boldsymbol{U}-\boldsymbol{U}_s=0 \tag{22}$$

where **U** and $\mathbf{U}_s$ are fluid and solid velocity respectively. So, $B(\mathbf{U})=\mathbf{U}=0$ for stationary cylinder.

The hydrodynamic force exerted on cylinder is approximated by

$$\boldsymbol{F}_{hydro}=\int_{0<\delta_\varepsilon^B<1}\delta_\varepsilon^B\int_A\left(p\boldsymbol{n}-\mu\left[\nabla\boldsymbol{u}+(\nabla\boldsymbol{u})^T\right]\boldsymbol{n}\right)dA d\delta_\varepsilon^B \tag{23}$$

where A is the isosurface of δ_ε^B and **n** is the unit normal vector on A.

2.5. Numerical solution method

The projection method (Chorin, 1968) is used for numerical solution. The liquid volume fraction of next time step is solved by advection function. For N–S equation, the pressure term, diffusion term, gravity, surface tension, wave-maker and wave absorber momentum source function are ignored, and estimated velocity **U*** of next time step is obtained by using the convection term:

$$\frac{\partial\alpha_l^{n+1}}{\partial t}=-\boldsymbol{U}^n\cdot\nabla\alpha_l^n \tag{24}$$

$$\frac{\partial(\rho\boldsymbol{U}^*)}{\partial t}=-\nabla\cdot(\rho\boldsymbol{U}^n\boldsymbol{U}^n) \tag{25}$$

where, the time derivative is discretized by the first order forward difference, and the convection term is discretized by the second order upwind scheme. Before solving the advection equation, the interface is approximated by piecewise linear interface calculation (PLIC) method (Tryggvason et al., 2006). The second order upwind scheme of x-coordinate velocity is as follows:

$$u_i^{n+1}=u_i^n-\Delta t\left(a^+u_x^-+a^-u_x^+\right)$$

$$a^+=max\left(u_i^n,0\right)$$

$$a^-=min\left(u_i^n,0\right) \tag{26}$$

$$u_x^-=\frac{3u_i^n-4u_{i-1}^n+u_{i-2}^n}{2\Delta x}$$

$$u_x^+=\frac{-u_{i+2}^n+4u_{i+1}^n-3u_i^n}{2\Delta x}$$

Secondly, the diffusion term is used to update the velocity from **U*** to **U****:

$$\frac{\partial(\rho\boldsymbol{U}^{**})}{\partial t}=\nabla\cdot(\mu\nabla\boldsymbol{U}^*) \tag{27}$$

in this step, the alternating direction implicit difference method (ADI) is used for discretization.

Thirdly, the pressure field p^{n+1} is solved based on pressure Poisson equation:

$$\nabla\cdot\left(\frac{1}{\rho^n}\nabla p^{n+1}\right)=\frac{\nabla\cdot\boldsymbol{U}^{**}}{\Delta t} \tag{28}$$

And the successive over-relaxation (SOR) iterative method is adopted to solve Poisson equation, and the discretization scheme is as follows:

$$p_i^{n+1}=\lambda\left[\frac{1}{\rho}\left(\frac{p_{i-1}^n+p_{i+1}^n}{\Delta x^2}+\frac{p_{j-1}^n+p_{j+1}^n}{\Delta y^2}+\frac{p_{k-1}^n+p_{k+1}^n}{\Delta z^2}\right)+\frac{\nabla\cdot\boldsymbol{u}^{**}}{\Delta t}\right]\Big/\frac{1}{\rho}\left(\frac{1}{\Delta x^2}+\frac{1}{\Delta y^2}+\frac{1}{\Delta z^2}\right)+(1-\lambda)p_i^n \tag{29}$$

Finally, through the projection step, the velocity field of next time step is updated by using pressure term and body force:

$$\frac{\boldsymbol{U}^{n+1}-\boldsymbol{U}^{**}}{\Delta t}=-\frac{1}{\rho^n}\nabla p^{n+1}+\boldsymbol{g}+\boldsymbol{f}_\sigma+\boldsymbol{f}_w+\boldsymbol{f}_d \tag{30}$$

where the surface tensor $\mathbf{f}_\sigma$ is solved by continuum surface force (Brackbill et al., 1992) (CSF) model and height function method (Guo et al., 2015; Malik et al., 2007).

3. Results and discussion

3.1. Regular wave generation

The numerical simulation of unidirectional regular wave is firstly conducted. Regular wave numerical tank is carried out by constructing wave-maker zone, working zone and wave absorbing area. Fig. 1 shows the section schematic of the numerical wave tank. When solving the N–S equation in the wave-maker region, the momentum source function f_{wx} and f_{wy} of Equations (11) and (12) is introduced. According to the numerical tests, in order to guarantee the consistency between the generated numerical regular wave and the expected wave, the length L_{gm} of the wave-maker zone needs to satisfy

$$0.18\lambda<L_{gm}<0.22\lambda \tag{31}$$

where, λ is the wavelength.

Numerical convergence tests are first conducted for regular wave with wave height $H=0.34$ m and angular frequency $\omega=3.04$ rad/s using Cartesian grid. For grid study, the reference simulation is based on cell number $N=5.67e6$, corresponding to roughly 150 cells per

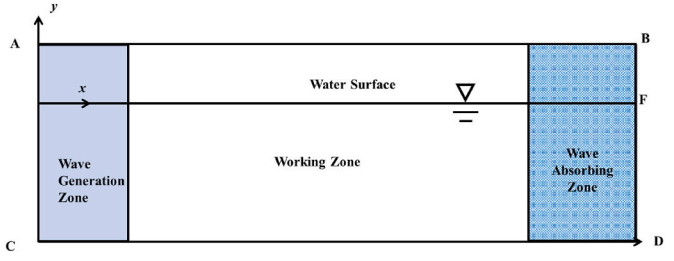

Fig. 1. Section scheme of numerical wave tank.

wavelength and 8 cells per wave height. The timestep for reference simulation is Δt = 5e-4s, corresponding to about 4000 timesteps per wave period. Simulations are conducted on two coarser grids with otherwise the same setup as the reference simulation, which are coarsened in both x-direction and y-direction by a factor 1.5 (resulting in roughly 100 cells per wavelength and 5 cells per wave height) and 2.25 (resulting in roughly 67 cells per wavelength and 4 cells per wave height), respectively. The monitored water surface elevation shown in Fig. 2(a) indicates that for the three grids, almost the same waves are generated and the differences in wave height are less than 9%. Even for the coarsest grid with only 4 cells per wave height, the wave profile and height can be effectively produced, showing that the numerical method is robust and only when the ratio of horizontal grid size to vertical grid size is appropriate, stable wave profiles can be guaranteed (Ha et al., 2013).

Besides, for timestep study, the reference simulation is based on Δt = 5e-4s and N = 1.12e6. Simulations are performed on two longer timesteps with otherwise the same setup as the reference simulation, which are Δt = 7.5e-4s and Δt = 1e-3s. As shown in Fig. 2(b), for Δt = 5e-4s and Δt = 7.5e-4s, nearly the same wave profiles are produced and the difference in wave height is less than 1%. Thus, the performance of the wave tank can be considered independent of the grid and timestep for practical purposes.

Fig. 3 shows the numerical wave profile distribution along x-coordinate of regular wave with wave height H = 0.34 m and angular frequency ω = 3.04 rad/s at different times. As shown in Fig. 3, the wave amplitude along x coordinate in working zone is basically consistent. In the wave absorbing area, the wave height gradually attenuates to zero, indicating that the wave absorbing method based on momentum source function has good wave absorption effect.

Fig. 4 shows the evolution process of wave surface displacement at the central point of the working zone. It can be seen from Fig. 4 that the wave surface displacement evolution is basically consistent with the third-order Stokes wave, and the amplitude and frequency of both are basically the same. Taking the static water surface as reference, the wave crest height is greater than the wave trough height, and the wave is no longer linear wave. The results show that although the wave-making momentum source function is based on the linear wave theory, under the continuous action of gravity, the wave propagating from the wave generation zone will develop into actual wave in the working zone, and the wave-making source function is mainly used as the initial disturbance to generate expected waves.

Fig. 5 shows the frequency spectrum of regular wave surface displacement, which is obtained by taking the average value of the frequency spectrum of displacement evolution at different mesh nodes on wave surface in the working area. It can be seen from Fig. 5 that the peak frequency of numerically generated wave is ω = 2.93 rad/s, while the frequency of expected regular wave is ω = 2.93 rad/s, and the error is less than 3%. The average amplitude of the numerical wave is A = 0.171 m, and the expected wave amplitude is A_{input} = 0.17 m, with an error less than 1%. The above results show that the wave-maker method

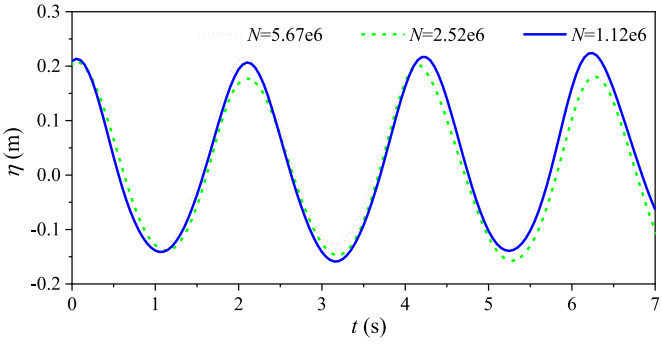

(a) Water surface elevation over time for different grid resolutions

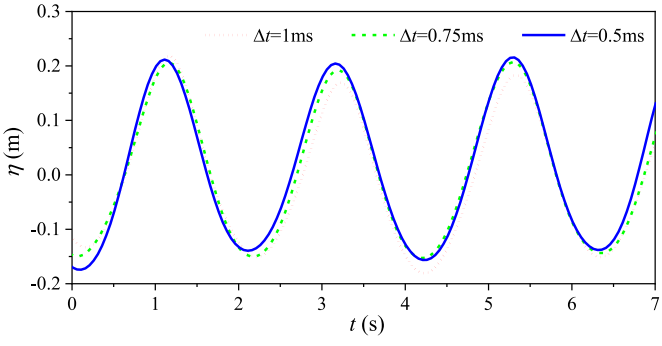

(b) Water surface elevation over time for different time steps

Fig. 2. Numerical convergence tests for a regular wave.

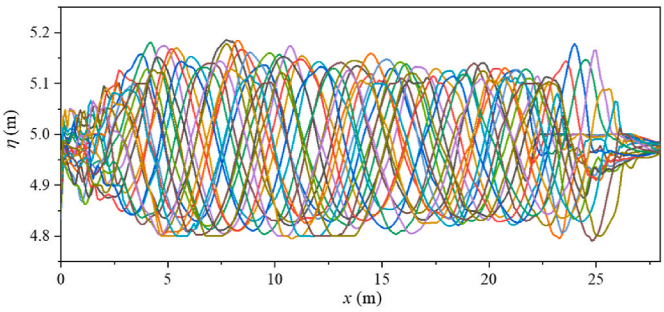

Fig. 3. Wave profile along x-coordinate of regular wave at different times.

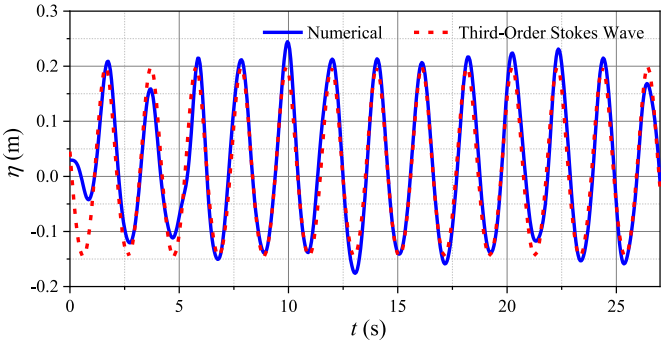

Fig. 4. Wave surface displacement of regular wave simulation and third-order Stokes wave.

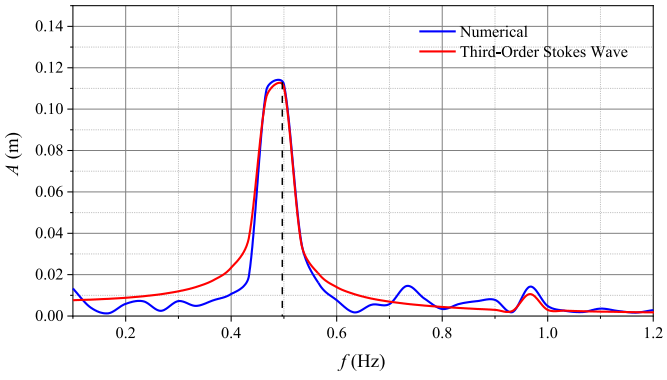

Fig. 5. Frequency spectrum of regular wave surface displacement.

Table 1
Results of regular wave simulation under different wave conditions.

	Wave Height/m			Angular Frequency/(rad/s)		
	Input	Num.	e_r/%	Input	Num.	e_r/%
Case 1	0.09	0.0932	3.5	3.04	3.07	1
Case 2	0.34	0.342	1	3.04	2.93	3
Case 3	0.5	0.488	2.4	3.04	2.945	3.1
Case 4	1.0	1.04	4	0.628	0.634	1
Case 5	1.5	1.77	18	0.628	0.636	1.3

based on the momentum source function can accurately simulate regular waves.

Table 1 shows the numerical results under different wave parameters. The length of wave-maker zone is always set to 0.22λ. As shown in Table 1, when the wave height H is not greater than 1 m, the wave height and frequency of numerical regular waves are relatively consistent with the input values. When the input wave height is greater than 1.5 m, the error of numerical wave height increases significantly. Therefore, when the wave height of the simulated wave increases gradually, in order to make the wave height consistent with the input values, the length of the wave-maker zone should be appropriately reduced.

3.2. Irregular wave generation

The actual ocean waves are random waves, whose wave energy is distributed at different frequencies and in different propagation directions. According to the Longuet-Higgins wave theory, the surface displacement of random waves can be expressed as the superposition of cosine waves with different frequencies and initial random phases. Therefore, the wave-maker momentum source function for random waves can be obtained by linear superposition of source function of regular waves with different frequencies,

$$f_{wx} = \sum_{n=1}^{N} a_n k_n g \frac{cos\ hk(y+h)}{cos\ hkh} sin(k_n x - \omega_n t + \varepsilon_n) \tag{32}$$

$$f_{wz} = -\sum_{n=1}^{N} a_n k_n g \frac{sin\ hk(y+h)}{cos\ hkh} cos(k_n x - \omega_n t + \varepsilon_n) \tag{33}$$

where, N is the total number of constituent waves, and a_n is the amplitude of the nth constituent wave; k_n and ω_n is the wave number and circular frequency of the nth constituent wave; t is time; ε_n is the initial random phase of the nth constituent wave, and is distributed uniformly and randomly in the range of $[0,2\pi)$. In this paper, $N = 100$ and ε_n Take the pseudo-random number generated by computer.

The random phase spectrum method (RPSM) (Borgman, 1969; Yuxiu, 1981) is used to calculate parameters in the momentum source function for random wave generation, and the JONSWAP spectrum is selected as the target spectrum. The JONSWAP spectrum needs to be divided into N parts to calculate wave parameters of every constituent wave, and if the frequency range is divided by the equal energy method, the amplitude of the nth constituent wave is given by

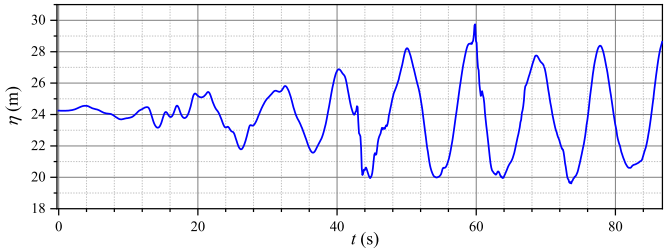

Fig. 6. Evolution of random wave surface displacement.

$$a_n = \frac{2m_0}{N} \tag{34}$$

where m_0 is the zeroth-order moment of JONSWAP spectrum.

Fig. 6 shows the displacement evolution at a fixed position on the random wave surface with spectral peak frequency $\omega_p = 0.7$ rad/s and significant wave height $H_s = 7.65$ m. As shown in Fig. 6, the displacement evolution has relatively obvious quasi-periodicity, which correspond to the peak frequency of the wave spectrum, and the amplitude of the wave component corresponding to the peak frequency is the largest. After 50s, the wave has developed completely, and the wave amplitude is almost stable. Fig. 7 shows the three-dimensional random wave surface at one moment in time and the corresponding surface displacement distribution at the middle section of NWT.

Fig. 8 shows the power spectrum of the aforementioned random wave surface displacement and JONSWAP spectrum. The peak value of the numerical random wave spectrum is basically consistent with that of JONSWAP spectrum. The numerical irregular wave spectral peak frequency is 0.675 rad/s, and the JONSWAP spectral peak frequency is 0.7 rad/s, indicating that numerical wave deviates slightly from the input wave. The significant wave height H_s of random waves could be calculated by the zeroth-order moment of wave spectrum:

$$H_s = 3.8\sqrt{m_0} \tag{35}$$

The significant wave height based on the numerical wave spectrum and JONSWAP spectrum are 7.65 m and 8.03 m respectively, and the deviation is less than 5%. As shown in Fig. 8, the amplitude of the numerical wave spectrum is smaller than that of the JONSWAP spectrum in high-frequency range, while in low-frequency range, the amplitude is larger, which may be related to the form of the momentum source function and the fluid viscosity. The wave-maker source function of the random wave is based on the inviscid linear wave theory. When viscous dissipation exists, the high-frequency component decays faster and the low-frequency component decays slower, resulting in the smaller amplitude of the high-frequency range and the larger amplitude of the low-frequency range in wave spectrum.

3.3. Horizontal wave force on different cylinders under regular wave

Based on the regular wave numerical tank, the force exerted on

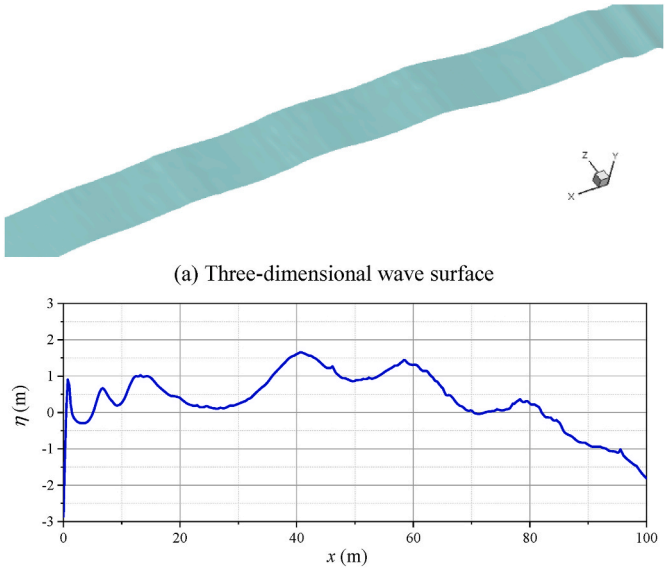

(a) Three-dimensional wave surface

(b) Wave profile along x-coordinate at midplane of NWT

Fig. 7. Three-dimensional wave surface and displacement distribution of random wave surface ($t = 18$s).

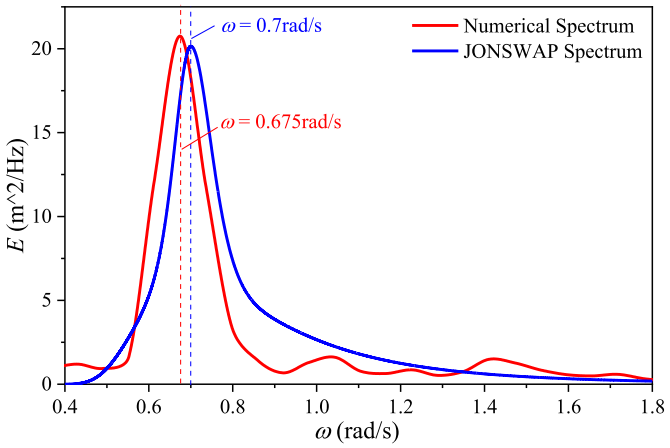

Fig. 8. Wave spectrum of numerical random wave and JONSWAP spectrum.

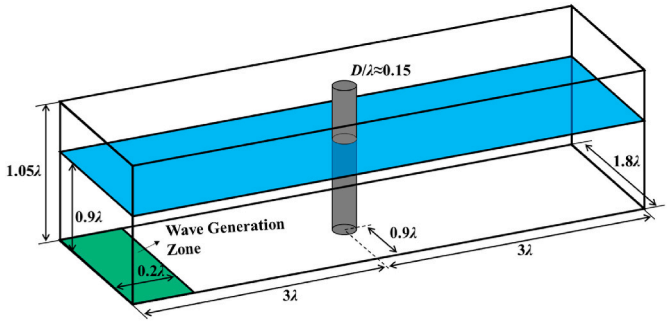

Fig. 9. Schematic diagram of numerical wave tank with FPC.

cylinder under regular wave field is studied. The interaction between regular wave and fully piercing cylinder (FPC) is firstly studied. The numerical model is shown in Fig. 9. For a L = 6λ long, $w = 1.9\lambda$ wide and $d = 0.9\lambda$ deep numerical wave tank, the wavemaker area length w_g is 0.2λ, the cylinder is set at the center of the tank, and the cylinder diameter $D = 0.126\lambda$. A target wave has wave height of $H = 0.45$ m, wavelength of $\lambda = 6.7$ m, frequency of $\omega = 3.04$ rad/s.

Fig. 10 shows the transverse wave force acted on FPC under regular wave and the result based on Morison equation (Dean and Dalrymple, 1991). As shown in Fig. 10, the wave force presents a periodicity and the period of the wave force evolution is consistent with the wave period. The maximum positive force on the cylinder is greater than the maximum negative transverse force. This is because the maximum positive force occurs near the wave crest, while the maximum negative force occurs near the wave trough. The liquid level near the wave crest is higher than the wave trough, and the viscous force on the cylinder near the wave crest is greater, so the maximum positive force on the cylinder

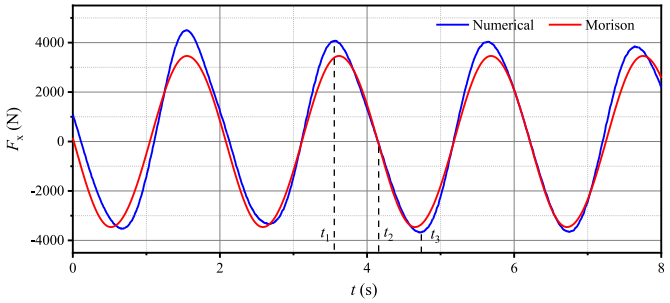

Fig. 10. Evolution of transverse force exerted on FPC with positive maximum, negative maximum and minimum values marked.

near the wave crest is greater than the maximum negative force near the wave trough.

The horizontal force evolution obtained by numerical simulation is basically consistent with that calculated by Morison equation, but the maximum positive and negative force obtained by simulation is greater than that calculated by Morison equation, which is related to the wave surface deformation. Morison equation is based on the assumption that the wave field will not be affected when cylinder is mounted at NWT, but

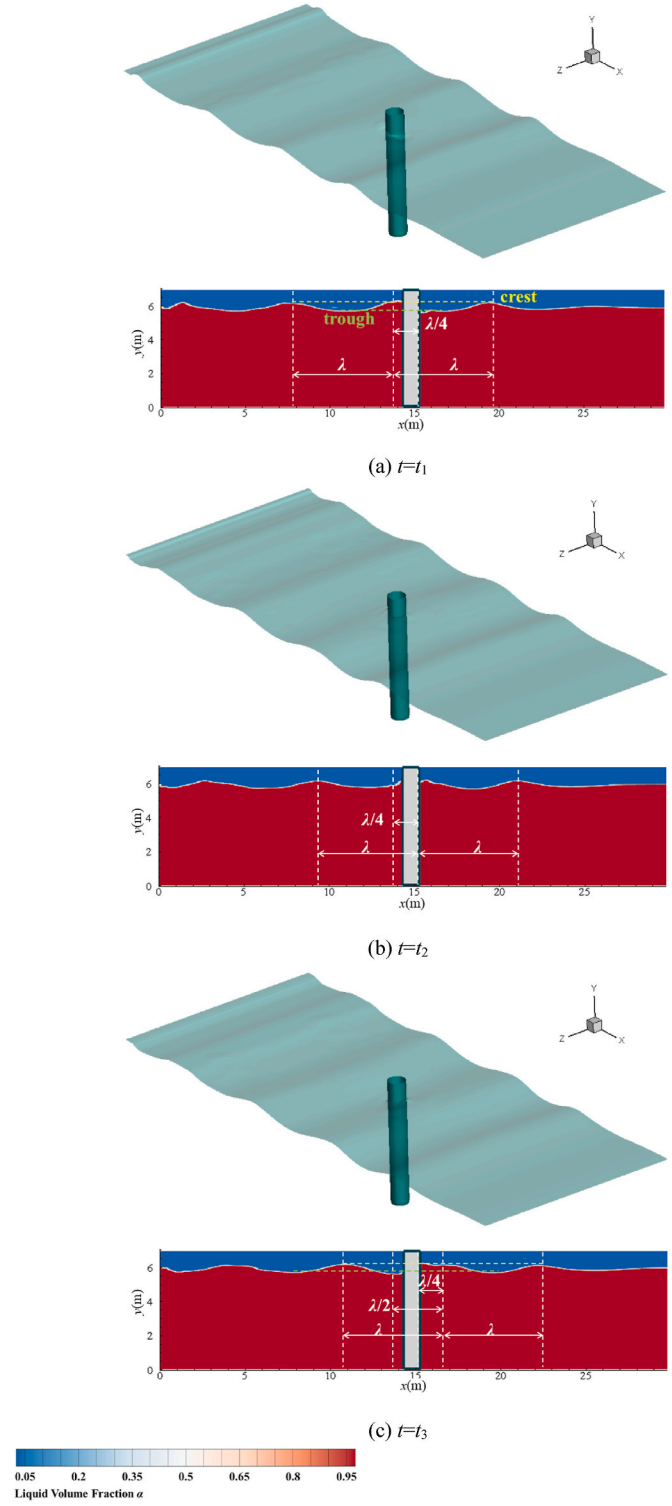

Fig. 11. Three-dimensional wave surface and liquid volume fraction distribution on the middle section ($H = 0.45$ m).

actually the wave profile has changed, especially near the cylinder, and the wave shape has changed significantly. Fig. 10 shows three moments t_1, t_2 and t_3 when the maximum positive force, the minimum force and the maximum negative force occur respectively. And Fig. 11 shows the three-dimensional wave surface and the volume fraction distribution of the liquid phase on the middle section of NWT corresponding to the three moments t_1, t_2 and t_3. When $t = t_1$, the transverse force reaches the maximum in the positive direction. It can be seen from Fig. 11(a) that the right end of the cylinder is at one-quarter of the wave length to the right of the wave crest. According to Morison equation, the transverse force mainly comes from the inertial force generated by fluid acceleration and the drag generated by fluid viscosity, and the inertial force is far greater than the viscous drag, as shown in Fig. 12. Fig. 12 shows the transverse force calculated based on Morison equation and the corresponding inertial force and viscous drag. If it is assumed that the cylinder has ignorable disturbance on the wave field, then theoretically when the center of the cylinder is at one-quarter of the wave length to the right of the wave crest (that's the right wave node, RWN), the inertial force reaches the maximum, and the viscous drag is zero. It can be seen from Fig. 12 that the viscous drag exerted on the cylinder is almost negligible, and the transverse force is mainly dominated by the inertial force. When the center of the cylinder is in front of the wave node to the immediate right of the wave peak (the wave node has not passed through the center of the cylinder), the viscous drag is in negative direction, contrary to the direction of the inertial force, and the transverse force on the cylinder is slightly less than the inertial force. When the center of the cylinder is behind the wave node (the wave node has passed through the center of the cylinder), the viscous drag is positive, and its direction is the same as the inertial force. The transverse force on the cylinder is slightly greater than the inertial force. However, it can be seen from Fig. 11(a) that when the wave node on the immediate right side of the wave crest passes through the cylinder, the wave profile near the cylinder is transformed obviously: the wave surface on the left side of the cylinder is higher than that without disturbance, and the wave surface on the right side of the cylinder is lower than that without cylinder. The existence of the cylinder results in an additional height difference between the front and rear sides of the cylinder. This additional height difference will make the inertial force on the cylinder greater than the inertial force calculated by Morison, so the maximum positive transverse force will also be greater. Based on Morison equation, when the center of the cylinder is at RWN, the inertial force reaches the maximum, and the total transverse force also reaches the maximum. However, in practice, due to the low flow velocity near the cylinder, the height difference between the front and rear of the cylinder is small, and the inertial force does not reach the peak. Therefore, the actual total transverse force on the cylinder does not reach the maximum when the center of the cylinder is at the wave node. As the wave continues to propagate forward, when the wave node reaches the right end of the cylinder, the inertial force on the cylinder reaches the maximum, and the transverse force on the cylinder reaches the maximum in the positive direction.

As shown in Figs. 11(b) and 10, when $t = t_2$, the center of the cylinder is located at about $D/2$ to the left of the wave crest, the positive viscous force is balanced with the negative inertial force, and the transverse force on the cylinder is zero. It can be seen from Fig. 12 that when the center of the cylinder is at the wave crest, the inertial force is basically zero, and the viscous drag reaches the maximum due to the maximum horizontal velocity, so the cylinder is subjected to positive transverse force at this time. Therefore, in order to make the total transverse force on the cylinder zero, negative inertial force is required, that is, the cylinder is located on the left side of the wave crest.

When $t = t_3$, the transverse force reaches the negative maximum. At this time, the rightmost end of the cylinder is at nearly one-quarter of the wave length to the immediate left of the wave crest (that's the left wave node, LWN). Similar to the situation where maximum positive force is reached, if the cylinder has little effect on the wave field, the transverse force should reach the negative maximum value when the center of the cylinder is located at LWN. However, due to the disturbance of the cylinder, an additional wave height difference between the front and rear of the cylinder exists, and the maximum negative force on the cylinder reaches after the LWN passes through the cylinder center for a distance (about $D/2$).

In addition, the force on a truncated cylinder (TC) under regular wave has also been studied. The schematic diagram of the cross-section of numerical wave tank is shown in Fig. 13. For a L = 4.7λ long, w = 0.31λ wide and d = 0.27λ deep numerical wave tank, the wavemaker area length w_g is 0.2λ, the cylinder is set at the center of the tank, the cylinder diameter D = 0.05λ, and the initial immersion depth of the cylinder is h = 0.1λ. A target wave has wave height of H = 0.41 m, wavelength of λ = 6.4 m, frequency of ω = 3.0 rad/s.

Fig. 14 shows the evolution of the transverse force on the truncated cylinder, and the curve based on Morison equation. Firstly, the accuracy of Morison equation for truncated cylinder is verified, and the validation data is based on the numerical results of Wang et al. (2022). As shown in Fig. 14, good agreement is achieved between the numerical results and Morison equation of H = 0.31 m, and the difference between the maximum positive force and maximum negative force is small because of small ratio of D/λ. And because the interference of the cylinder on the wave field is relatively small, the transverse force calculated by Morison is close to the actual force.

The force evolution of the truncated cylinder is also basically consistent with that calculated by Morison equation for wave height H = 0.41 m. As shown in Fig. 14, three moments t_1, t_2 and t_3 are marked when the maximum positive force, the minimum force and the maximum negative force occur respectively. Moreover, Fig. 15 shows

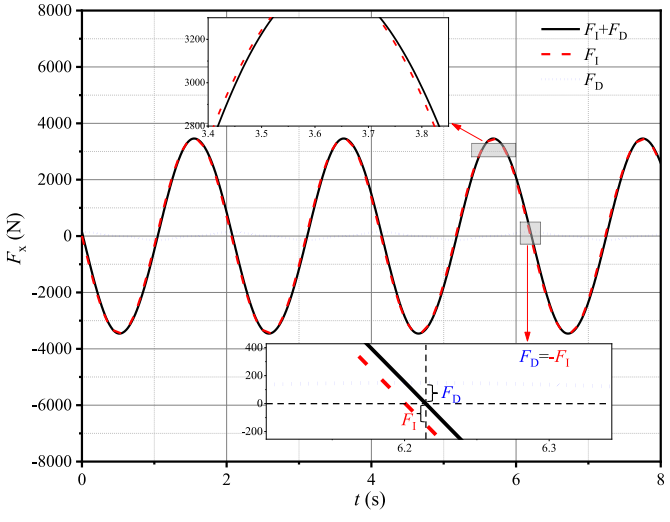

Fig. 12. The lateral force on FPC based on Morison equation and the corresponding inertial force F_I and viscous drag F_D (H = 0.45 m).

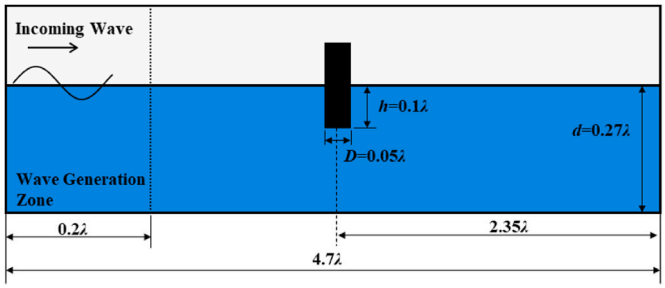

Fig. 13. Schematic diagram of the middle section of NWT with TC.

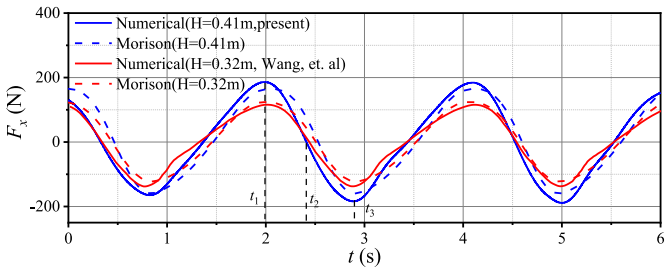

Fig. 14. Evolution of transverse force exerted on TC with positive maximum, negative maximum and minimum values marked.

the three-dimensional wave surface and the distribution of the liquid volume fraction on the middle section of NWT to above three moments. When $t = t_1$, the horizontal force acting on the TC reaches the maximum in the positive direction. It can be seen from Fig. 15(a) that the rightmost end of the truncated cylinder is at $\lambda/8$ to the right of the wave crest. Fig. 16 shows the lateral force on the TC based on Morison equation and the corresponding inertia force and viscous drag. The results, shown in Figs. 16 and 12, demonstrate that the transverse force on TC is still dominated by the inertial force, but the influence of viscous drag increases in comparison to FPC. Therefore, the maximum transverse force on TC does not occur when the inertial force reaches the positive maximum, that is, when the center of the truncated cylinder coincides with the RWN. According to the results of Morison equation in Fig. 16, when the wave profile is not disturbed by cylinder, the maximum

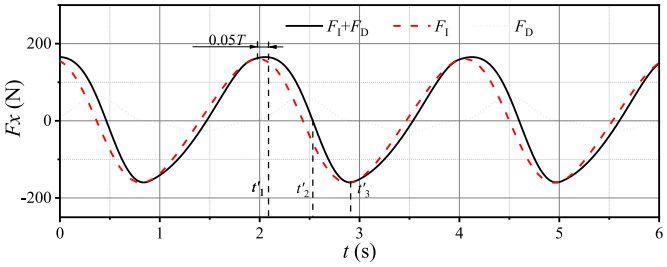

Fig. 16. The lateral force on TC based on Morison equation and the corresponding inertial force F_I and viscous drag F_D ($H = 0.41$ m).

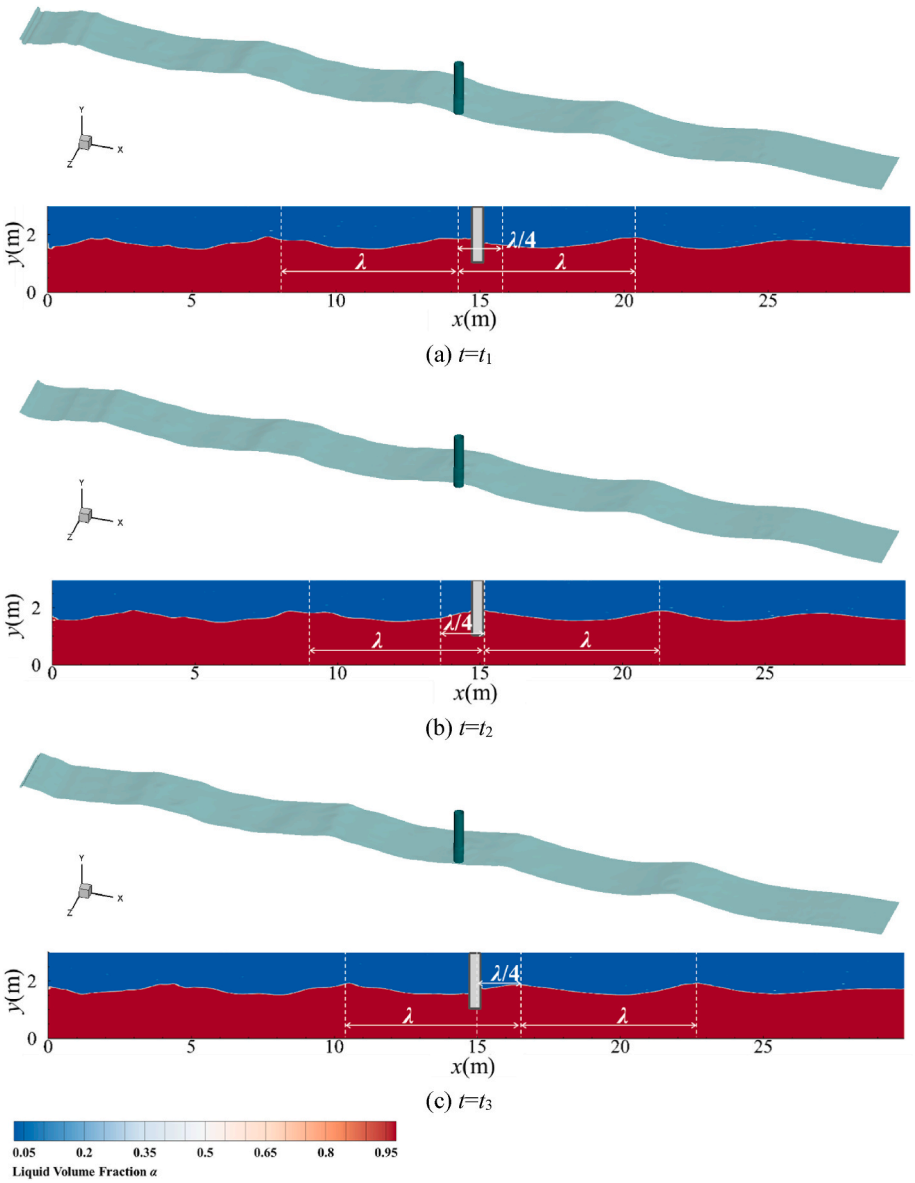

Fig. 15. Three-dimensional wave surface and liquid volume fraction distribution on the middle section ($H = 0.41$ m).

transverse force lag lags behind maximum inertial force about 0.05T. In addition, due to wave deformation near the truncated cylinder, the maximum horizontal force on TC occurs at about $\lambda/8$ to the right of wave crest, and TC is relatively closer to the wave crest compared with FPC.

As shown in Figs. 15(b) and 14, when $t = t_2$, the center of the truncated cylinder is located at about $D/2$ to the left of the wave crest, and the transverse force is zero. Fig. 16 shows that when the inertia force is zero (the center of the truncated cylinder is near the wave crest), the viscous drag reaches the maximum due to the high horizontal flow velocity, and at this moment the cylinder is subjected to a positive transverse force. Therefore, in order to realize the minimum transverse force, a negative inertial force is required, that is, located on the immediate left of wave crest. Similar to FPC, when $t = t_3$, the transverse force on the truncated cylinder reaches the negative maximum and the rightmost end of TC is around at LWN. In other words, because of the disturbance of truncated cylinder on wave surface, the maximum negative transverse emerges about $D/2$ after the LWN passes through the cylinder center.

4. Conclusion

The momentum source function for regular and random waves are constructed based on the linear wave theory, and the numerical wave tank is established by combining the incompressible viscous N–S equation and VOF method. Regular waves with different wave parameters and random wave based on JONSWAP spectrum are simulated and verified, and the wave force characteristics on FPC and TC under regular wave are studied by combining the boundary data immersion method. When the length of wavemaker is taken as $L_{gm} = 0.22\lambda$ and regular wave amplitude is less than 1.5 m, the amplitude and frequency of numerical wave are in good agreement with the expected wave. When the wave amplitude is greater than 1.5 m, the amplitude of the numerical regular wave is larger than the expected, while the frequency is still satisfactory. Therefore, the length of the wavemaker zone should be appropriately reduced to obtain the desired amplitude.

Random waves can be generated by the linear superposition of the regular wave's momentum source function. The wave spectrum of the numerical random wave is almost consistent with the expected JONSWAP spectrum, and the significant wave height is also basically the same. However, the energy of the high-frequency component in numerical spectrum is less than the expected, while the low-frequency component is higher than the expected value, which is related to the energy dissipation caused by fluid viscosity.

The transverse force on the cylinder obtained by regular wave's NWT is consistent with Morison equation. The transverse force is dominated by the inertial force, but because of the interference of cylinder with wave profile, the positive or negative maximum of the transverse force occurs after the right or left wave node passes through the center of the cylinder. Compared with the FPC, the viscous drag accounts for a larger proportion of the transverse force on the TC.

Declaration of competing interest

The authors declare that they have no known competing financial interests or personal relationships that could have appeared to influence the work reported in this paper.

Data availability

Data will be made available on request.

Acknowledgements

This work is supported by the National Key R&D Program of China (Grant No. 2022YFB3303500).

References

Ben-long, W., Hua, L., 2005. Higher order boussinesq-type equations for water waves on uneven bottom. Appl. Math. Mech. 26 (6), 714–722.
Benxia, L., Yuxiu, Y., Ningchuan, Z., 2004. Development of 2-D numerical random wave tank and its application. Mar. Sci. Bull. 23 (5), 1–9.
Borgman, L.E., 1969. Directional spectra models for design use. In: Offshore Technology Conference, Dallas, Texas.
Brackbill, J.U., Kothe, D.B., Zemach, C., 1992. A continuum method for modeling surface tension. J. Comput. Phys. 100 (2), 335–354.
Choi, J., Yoon, S.B., 2009. Numerical simulations using momentum source wave-maker applied to rans equation model. Coast. Eng. 56 (10), 1043–1060.
Chorin, A.J., 1968. Numerical solution of the Navier-Stokes equations. Math. Comput. 22 (104), 745.
Dean, R.G., Dalrymple, R.A., 1991. Water Wave Mechanics for Engineers and Scientists. World Scientific.
Dommermuth, D.G., Yue, D.K.P., 1987. A high-order spectral method for the study of nonlinear gravity waves. J. Fluid Mech. 184, 267–288.
Guo, X., Wang, B., Liu, H., 2012. Numerical simulation of irregular wave overtopping against a smooth sea dike. China Ocean Eng. 26 (1), 153–166.
Guo, Z., Fletcher, D.F., Haynes, B.S., 2015. Implementation of a height function method to alleviate spurious currents in cfd modelling of annular flow in microchannels. Appl. Math. Model. 39 (16), 4665–4686.
Ha, T., Lin, P., Cho, Y., 2013. Generation of 3D regular and irregular waves using Navier-Stokes equations model with an internal wave maker. Coast. Eng. 76, 55–67.
Houtani, H., Waseda, T., Fujimoto, W., Kiyomatsu, K., Tanizawa, K., 2018. Generation of a spatially periodic directional wave field in a rectangular wave basin based on higher-order spectral simulation. Ocean Eng. 169, 428–441.
Lin, P., Liu, P.L.F., 1999. Internal wave-maker for Navier-Stokes equations models. J. Waterw. Port, Coast. Ocean Eng. 125 (4), 207–215.
Lin, P., Liu, P.L.F., 2004. Discussion of "vertical variation of the flow across the surf zone". Coast. Eng. 50 (3), 161–164.
Malik, M., Fan, E.S., Bussmann, M., 2007. Adaptive vof with curvature-based refinement. Int. J. Numer. Methods Fluid. 55 (7), 693–712.
Martínez-Ferrer, P.J., Qian, L., Ma, Z., Causon, D.M., Mingham, C.G., 2018. Improved numerical wave generation for modelling ocean and coastal engineering problems. Ocean Eng. 152, 257–272.
Perić, R., Abdel-Maksoud, M., 2015. Generation of free-surface waves by localized source terms in the continuity equation. Ocean Eng. 109, 567–579.
Tryggvason, G., Esmaeeli, A., Lu, J., Biswas, S., 2006. Direct numerical simulations of gas/liquid multiphase flows. Fluid Dynam. Res. 38 (9), 660–681.
Wang, B., Li, Y., Wu, F., Gao, S., Yan, J., 2022. Numerical investigation of wave run-up and load on fixed truncated cylinder subjected to regular waves using openfoam. Water-Sui. 14 (18), 2830.
Wang, W., Gao, Z., 2022. On the accuracy of large-steepness regular wave generation, propagation and run-up on a cylinder. Ocean Eng. 251, 111088.
Wei, G., Kirby, J.T., 1995. Time-dependent numerical code for extended Boussinesq equations. J. Waterw. Port, Coast. Ocean Eng. 121 (5), 251–261.
Wei, G., Kirby, J.T., Sinha, A., 1999. Generation of waves in Boussinesq models using a source function method. Coast. Eng. 36 (4), 271–299.
West, B.J., Brueckner, K.A., Janda, R.S., Milder, D.M., Milton, R.L., 1987. A new numerical method for surface hydrodynamics. J. Geophys. Res. 92 (C11), 11803.
Weymouth, G.D., Yue, D.K.P., 2011. Boundary data immersion method for cartesian-grid simulations of fluid-body interaction problems. J. Comput. Phys. 230 (16), 6233–6247.
Xu, G., Zhou, Y., Yan, S., Zhang, N., 2022. Numerical investigation of wave amplitude spectra effects on focusing wave generation. Ocean Eng. 265, 112550.
Yuxiu, Y., 1981. Numerical simulation and prediction of ocean wave. J. Dalian Univ. Technolgy 48 (2), 84–90.